

Optical biopsy with long-range nondiffracting beams

Ervin Goldfain

Welch Allyn Inc, Skaneateles Falls, NY 13153

ABSTRACT

Most current configurations for optical biopsy contain fiber optic bundles at both the delivery and receiving ends of the optical system. Some layouts include distal lenses to either collimate or focus the incident light at various depth locations across the tissue. The inherent beam divergence, along with the highly scattering nature of the living tissue, are known to limit the penetration depth of the probe and the spatial or temporal resolution of the detected signal.

In this work we study a novel modality for tissue illumination based on the use of long-range nondiffracting beams (LRNB). LRNB represent narrow-width light pencils with a constant or linearly varying axial intensity that propagate over large distances without diffractive spreading. Recent tests have demonstrated that LRNB exhibit insignificant intensity distortions when operated as beacon beams through atmospheric turbulence. Our numerical and software simulations show that LRNB may offer the potential for larger penetration depth and enhanced contrast over setups using conventional laser beams. Clinical applications include diagnosis, laser surgery and photodynamic therapy.

Keywords: optical biopsy, tissue imaging, biomedical spectroscopy, nondiffracting beams, Bessel beams, axicon.

1. INTRODUCTION

Standard beam delivery systems for optical biopsy are based upon fiber optic bundles or optical components such as conventional lenses or light concentrators. The probing beam is either collimated or focused on various depth locations inside the tissue volume. It is well known that the inherent beam divergence, along with the occurrence of multiple photon scattering and absorption events inside the tissue, degrade the spatial and temporal resolution of the detected signal.

A number of approaches have been introduced to offset this challenge, including confocal imaging and spectroscopy,^{1,2} phase-shift detection,^{3,4} and time-gated techniques using low-coherence interferometry⁵⁻⁹.

The main drawback of these approaches is that, for thick tissue, a vast majority of transmitted photons is discarded and the scarcity of detected light with the shortest propagation length limits the achievable gain in resolution^{10,11}. For instance, time-gated mammography generally fails to distinguish an inhomogeneity smaller than approx. 10 mm., which falls short of the resolution required for a routine screening of breast disease¹⁰. In thick tissue, an ultrashort pulse will typically broaden by many orders of magnitude during a detection time window comparable to the duration of the probing pulse¹¹.

We report in this work a novel strategy for tissue illumination based on the use of long-range nondiffracting beams (LRNB). LRNB are produced by using several techniques^{12,13} such as placing an annular ring in the focal plane of a well corrected lens, via phase filters, refractive or holographic axicons, or spherically aberrated optical systems. Recent experiments have demonstrated that LRNB exhibit minor intensity distortions when used as beacon beams through atmospheric turbulence¹⁴. It is worth mentioning here that acoustic nondiffracting beams have been studied in conjunction with 2D and 3D ultrasound imaging¹⁵.

The paper is organized as follows: the first section briefly describes the theory underlying LRNB, the second section deals with a numerical comparison between conventional and LRNB excitation modes as applied to the steady-state fluorescence spectroscopy of thick tissue. The third section reports results of a Monte Carlo simulation comparing time-gated imaging under conventional and LRNB illumination. Conclusions and future challenges are outlined in the last section.

2. OPTICAL DESCRIPTION OF THE NONDIFFRACTING BEAM

The nondiffracting beam belongs to a class of solutions of the wave equation which are invariant with respect to diffraction from one plane of propagation to the next. The simplest nontrivial example of a nondiffracting beam is the zero-order Bessel wave¹⁶:

$$E(x, y, z, t) = E_0 \cdot J_0(\alpha \cdot \rho) \cdot \exp[-i \cdot (\omega \cdot t - \beta \cdot z)] \quad (1)$$

in which :

$$0 \leq \alpha \leq \left(\frac{2 \cdot \pi}{\lambda} \right) \quad (2)$$

$$\rho^2 = x^2 + y^2$$

with "x,y" denoting beam coordinates in a plane normal to the propagation direction "z", "λ" being the wavelength, "t" the time, "ω" the angular frequency, "E₀" the electric field amplitude and J₀ the zero-order Bessel function. The beam parameter "β" satisfies the relationship:

$$\beta^2 = \left(\frac{2 \cdot \pi}{\lambda} \right)^2 - \alpha^2 \quad (3)$$

Fig.1 shows the plot of the Bessel beam in the (x,y) plane. The central peak has a width proportional to "α" and is generally surrounded by several concentric rings that may be suppressed by truncating the beam with annular stops¹⁷.

It can be shown that, if the beam is generated through apertures with custom transmission functions^{18,19,20}, the axial beam intensity becomes linearly dependent on the propagation distance according to:

$$I(x, y, z) = I_0 \cdot (a + b \cdot z) \cdot [J_0(\alpha \cdot \rho)]^2 \quad (4)$$

in which:

$$I(x, y, z) = (|E(x, y, z, t)|)^2 \quad (5)$$

$$I_0 = (E_0)^2$$

and where the real coefficients "a" and "b" satisfy the condition:

$$a + b \cdot z > 0 \quad (6)$$

The range over which the axial beam intensity yields a uniform or a linearly varying profile follows the construction of the beam forming optics. Controlling the amount of spherical aberration introduced by the lens system or the cone angle of the linear axicon are typical examples of how a desired distance range may be achieved in practice^{20,21}.

3. SIMULATION RESULTS

3.1 Steady-state fluorescence spectroscopy in thick tissue

In this section we perform numerical evaluations of the fluorescent signal emitted by a generic fluorophore source under steady-state conventional (Gaussian beam) and LRNB excitation. It is assumed that the fluorophore is deeply buried in an isotropic semi-infinite slab of homogeneous tissue which can be modeled as a highly scattering medium.

To make the comparison relevant, it is assumed that both conventional and LRNB ballistic components of the excitation light are focused on the fluorophore at depth ($-z_f$) and that both focal spots are subjected to the same average intensity (measured in flux per unit area).

Referring to fig. 2 and taking into account (4), the intensity distribution for the ballistic component of the excitation light attenuated by scattering and absorption losses is described by²²:

$$I(\rho, z)_G = I_{0,G} \left[\frac{w_0(z_0)}{w(z)} \right]^2 \cdot \exp \left[-2 \cdot \left(\frac{\rho}{w(z)} \right)^2 \right] \cdot \exp[-\mu_t \cdot (z + z_f)] \quad (\text{Gaussian beam}) \quad (7)$$

$$I(\rho, z)_{LRNB} = I_{0,LRNB} \left[a + b \cdot (z + z_f) \right] \cdot \left[J_0(\alpha \cdot \rho) \right]^2 \cdot \exp[-\mu_t \cdot (z + z_f)] \quad (\text{LRNB})$$

In the above $w_0(z_0)$ stands for the Gaussian beam waist at the depth of focus " z_0 ":

$$w_0(z_0) = \sqrt{\frac{\lambda \cdot z_0}{\pi}} \quad (8)$$

$w(z)$ is the waist at any arbitrary depth " z ":

$$w(z) = w_0(z_0) \cdot \sqrt{1 + \left(\frac{z}{z_0} \right)^2} \quad (9)$$

and " μ_t " is the total transport coefficient. Setting equal average intensity of the focal spot for both ballistic modes amounts to integrating (7) over the radial coordinate ρ and dividing by the linear extent of the focal spot, that is:

$$\frac{\int_0^{\rho_0} I(\rho, 0)_{LRNB} d\rho}{\rho_0} = \frac{\int_0^{w_0(z_0)} I(\rho, 0)_G d\rho}{w_0(z_0)} \quad (10)$$

in which the integrated intensity is carried out at $z = 0$ and ρ_0 represents the effective radius of the LRNB focal spot. In the framework of diffusion theory it can be shown that the beam intensity at depth ($-z_f$) may be expressed as²³:

$$I(-z_f) = I_s \cdot K(-z_f) \quad (11)$$

where I_s is the beam intensity on the tissue surface and $K(-z_f)$ is a depth-dependent function. For a given excitation beam intensity, the local fluorescence emission rate is represented by the product:

$$f(-z_f) = \gamma \cdot I(-z_f) \cdot \mu_{a,f,\lambda}(-z_f) \quad (12)$$

with γ denoting the quantum fluorescence yield and $\mu_{a,f,\lambda}(-z_f)$ the fluorophore absorption coefficient for the excitation wavelength λ . Combining the above, the fluorescent signal reaching the tissue surface takes the form²³:

$$F(0) = \int_0^\infty E(0, -z_f) \cdot f(-z_f) dz_f = \gamma \cdot I_s \cdot \int_0^\infty E(0, -z_f) \cdot K(-z_f) \cdot \mu_{a,f,\lambda}(-z_f) dz_f \quad (13)$$

where $E(0, -z_f)$ is the total intensity that reaches a single point on the tissue surface. This quantity depends on fluorophore location and on the optical properties of the tissue. Let "g" denote the ratio of the fluorescent signal produced under LRNB excitation to the one produced by Gaussian excitation. From (7) and (13) it follows that:

$$g = \frac{F_{LRNB}(0)}{F_G(0)} = \frac{I_{s,LRNB}}{I_{s,G}} = \frac{I_{0,LRNB} \cdot a \cdot [J_0(\alpha \cdot \rho)]^2}{I_{0,G} \left[\frac{w_0(z_0)}{w(z_f)} \right]^2 \cdot \exp \left[-2 \cdot \left(\frac{\rho}{w(z_f)} \right)^2 \right]} \quad (14)$$

Fig. 3 represents plots of the gain "g" versus fluorophore depth "zf" (in absolute value) corresponding to the following choice of constructive parameters ($\lambda = 920$ nm, $I_{0,LRNB} = I_{0,G} = a = 1$) :

$\alpha_1 = 18.781 \text{ mm}^{-1}$	$w_{0,1} = .125 \text{ mm}$	$\rho_{0,1} = .100 \text{ mm}$
$\alpha_2 = 15.026 \text{ mm}^{-1}$	$w_{0,2} = .150 \text{ mm}$	$\rho_{0,2} = .125 \text{ mm}$
$\alpha_3 = 12.526 \text{ mm}^{-1}$	$w_{0,3} = .180 \text{ mm}$	$\rho_{0,3} = .150 \text{ mm}$

The graph indicates that , for a given fluorophore depth, the gain "g" scales up with the reduction in the focal spot size " ρ_0 ". This may be an attractive alternative for the spectroscopy of deeply buried small-size fluorophores, which may otherwise be inaccessible with conventional pencil-like beams.

3.2 Time-gated imaging through thick tissue

3.2.1 Comparison of the depth-dependent intensity distributions

In this section we use (7) to study an example of time-gated imaging through thick tissue. Assuming that both the diffusive and the snake components of the illumination beam are rejected via time-gating, we again set the focal spot intensity to be equal on average for the ballistic component, according to (10). In addition, we assume that both beams are being focused halfway through tissue thickness and have a comparable spot diameter. This additional assumption puts the Gaussian and the LRNB modes on equal footing insofar as the ability to generate a resolvable transmitted signal or an acceptable imaging contrast.

Figs. 4 and 5 show the 3D intensity plots corresponding to the ballistic components of the LRNB and Gaussian modes at the focal spot ($z = 0$) and deeper depth locations ($z > 0$). The vertical axis indicates intensity, the horizontal axis contained in the intensity cross section denotes the radial coordinate (ρ) and the third axis corresponds to the depth coordinate (z). The inhomogeneity is buried at $z_i = 50$ mm below the tissue surface. Note that all units have been normalized to a set of arbitrary values. The parameters of this numerical simulation are chosen as follows:

$$\begin{aligned} \lambda &= 920 \text{ nm} & w_0 &= .125 \text{ mm} \\ I_{0,LRNB} &= I_{0,G} = 1 & \rho_0 &= .100 \text{ mm} \\ a &= 0, b = .02 \text{ mm}^{-1} & \mu_t &= 1.04 \text{ mm}^{-1} \\ \alpha &= 18.781 \text{ mm}^{-1} & z_i &= 50 \text{ mm} \end{aligned}$$

3.2.2 Monte Carlo raytracing

In this section we show comparative results of a statistical raytracing simulation of time-gated imaging through thick tissue (fig. 6). Using a commercially available software package, a large number of raypaths ($2 \cdot 10^6$) is randomly traced through a stack of two diffusing layers with a fully absorbing inhomogeneity embedded at half of the overall thickness. The Gaussian beam is delivered through a planoconvex lens and the nondiffracting beam is generated using a refractive axicon . The comparison between the two illumination modes is based upon the contrast function, which is defined as:

$$C(\%) = \frac{I_{\max} - I_{\min}}{I_{\max}} \cdot 100 \quad (15)$$

in which I_{\max} and I_{\min} stand for the maximum and minimum peaks of the detected intensity distribution. As before, we rely on the assumption that time-gating is fully efficient in the sense that only the ballistic component survives detection. The focal spot intensity and size are set equal for both illumination modes. The inhomogeneity diameter is denoted by "d" and the thickness of each layer by "t". The axicon profile is described by the linear function:

$$z = (-.003) \cdot r \quad (16)$$

where "z" and "r" are the axial and radial coordinates of the axicon surface. The rest of simulation parameters are as follows:

<u>input source</u> : step-index fiber optic, core diameter .500 mm	<u>operating wavelength</u> : $\lambda = 700$ nm
<u>illumination numerical aperture</u> : .25	<u>emitted flux</u> : 100 mW
<u>overall tissue thickness</u> : 100 mm (2.t)	<u>focal spot size</u> : 3 mm
<u>focal spot intensity</u> : .025 lumen/mm ²	<u>total transport coefficient</u> (μ_t): 1.04 mm ⁻¹

4. CONCLUSIONS

A side by side analysis of the Gaussian beam and LRNB illumination modes has been developed. Simulation results point out that LRNB may be superior in terms of penetration depth and signal contrast for the characterization and diagnosis of thick tissue. Additional modeling and experimental work are required to validate these preliminary findings. One is specifically interested in further exploration of clinical benefits, dynamic range, as well as potential limitations associated with the LRNB modality.

5. REFERENCES

1. D. S. Dilworth, E. N. Leith and J. L. Lopez, "Imaging absorbing structures within thick diffusing media", *Appl. Opt.* **29**, 691-698 (1990).
2. D. S. Dilworth, E. N. Leith and J. L. Lopez, "Three-dimensional confocal imaging of objects embedded within thick diffusing media", *Appl. Opt.* **30**, 1796-1803 (1991).
3. M. S. Patterson, J. D. Moulton, B. C. Wilson, K. W. Berndt and J. R. Lakowicz, "Frequency-domain reflectance determination of the scattering and absorption properties of tissue", *Appl. Opt.* **30**, 4474-4476 (1991).
4. J. B. Fiskin and E. Gratton, "Propagation of photon-density waves in strongly scattering media containing an absorbing semi-infinite plane bounded by a straight line", *JOSA A* **10**, 127-140 (1993).
5. H. P. Chiang, W. S. Chang and J. Wang, "Imaging through random scattering media by using cw broadband interferometry", *Opt. Lett.* **18**, 546-548 (1993).
6. M. R. Hee, J. A. Izatt, J. M. Jacobson and J. G. Fujimoto, "Femtosecond transillumination optical coherence tomography", *Opt. Lett.* **18**, 950-952 (1993).
7. M. E. Brezinski *et al.*, "Optical Biopsy with Optical Coherence Tomography", *Advances in Optical Biopsy and Optical Mammography*, Annals of the New York Academy of Sciences, New York, vol. **838**, 68-74 (1998).
8. J. G. Fujimoto *et al.*, "New Technology for High-Speed and High-Resolution Optical Coherence Tomography", *Advances in Optical Biopsy and Optical Mammography*, Annals of the New York Academy of Sciences, New York, vol. **838**, 95-107 (1998).
9. B. E. Bouma *et al.*, "High-resolution optical coherence tomographic imaging using a mode-locked Ti:Al₂O₃ laser source", *Opt. Lett.* **20**, 1486-1488 (1995).
10. J. C. Hebden and Simon R. Arridge, "Imaging through scattering media by the use of an analytical model of perturbation amplitudes in the time domain", *Appl. Opt.* **35**, 6788-6796 (1996).
11. J. C. Hebden, D. J. Hall, M. Firbank and D. T. Delpy, "Time-resolved optical imaging of a solid tissue-equivalent phantom" *Appl. Opt.* **34**, 8038-8047 (1995).
12. R. M. Herman and T. A. Wiggins, "Production and uses of diffractionless beams", *JOSA A* **8**, 932-942 (1991).
13. R. M. Herman and T. A. Wiggins, "High-efficiency diffractionless beams of constant size and intensity", *Appl. Opt.* **33**, 7297-7306 (1994).
14. T. Aruga *et al.*, "Nondiffracting narrow light beam with small atmospheric turbulence-influenced propagation", *Appl. Opt.* **38**, 3152-3156 (1999).
15. This reference is located at <www.ifi.uio.no/~fox/abstract.htm>.
16. W. Lauterborn, T. Kurz and M. Wiesenfeldt, "*Coherent Optics*", Springer-Verlag, Berlin Heidelberg, 24, (1995).
17. Z. Jaroszewicz, J. Sochacki, A. Kolodziejczyk and L. R. Staronski, "Apodized annular-aperture logarithmic axicon: smoothness and uniformity of intensity distributions", *Opt. Lett.* **18**, 1893-1895, (1993).

18. Z. Jiang, Q. Lu and Z. Liu, "Propagation of apertured Bessel beams", *Appl. Opt.* **34**, 7183-7185, (1995).
19. S. Y. Popov, A. T. Friberg, "Linear axicons in partially coherent light", *Opt. Eng.* **34**, 2567-2573, (1995).
20. R. M. Herman and T. A. Wiggins, "Apodization of diffractionless beams", *Appl. Opt.* **31**, 5913-5915, (1992).
21. T. Aruga and S. W. Li, "Super high resolution for long-range imaging", *Appl. Opt.* 2795-2799, (1999).
22. J. Ying, F. Liu and R. R. Alfano, "Spatial distribution of two-photon-excited fluorescence in scattering media", *Appl. Opt.* **38**, 224-229, (1999).
23. T. J. Farrel *et al.*, "Modeling of photosensitizer fluorescence emission and photobleaching for photodynamic therapy dosimetry", *Appl. Opt.* **37**, 7168-7183, (1998).

6. PLOTS

FIG. 1

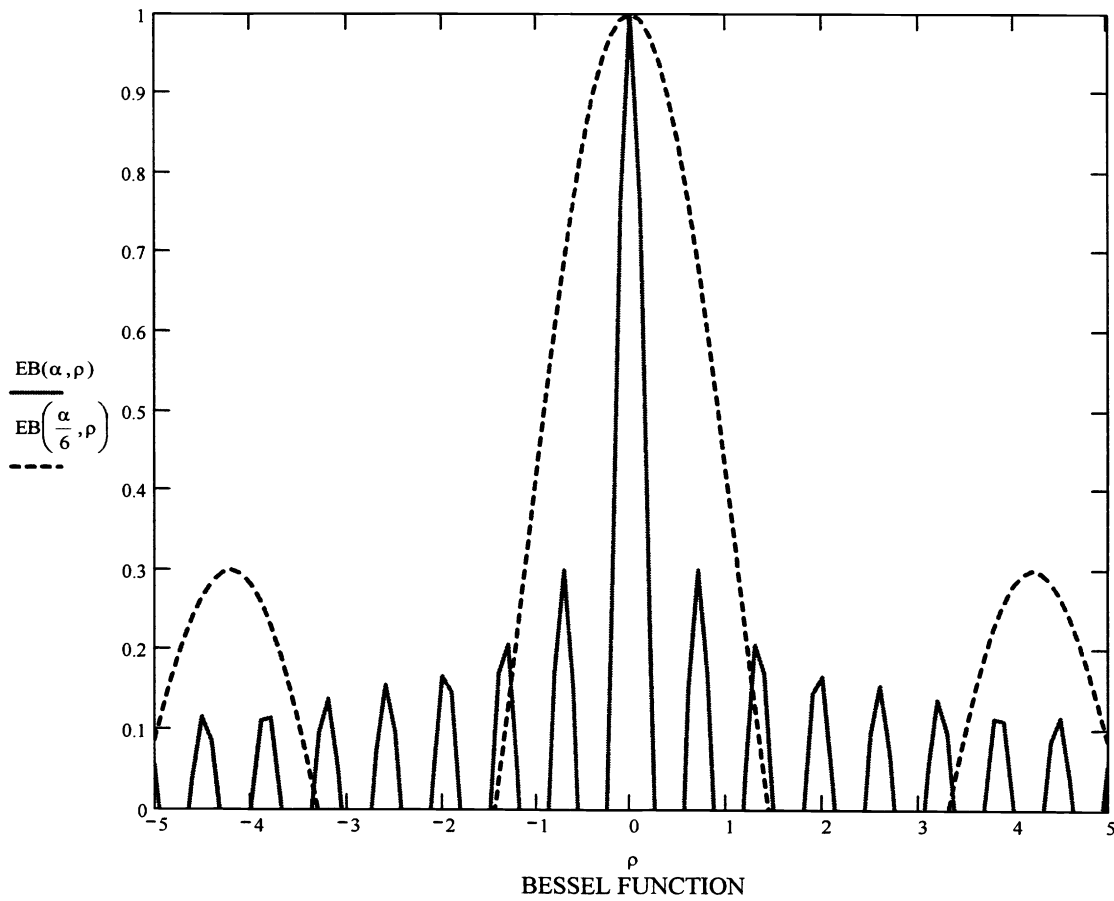


FIG. 2

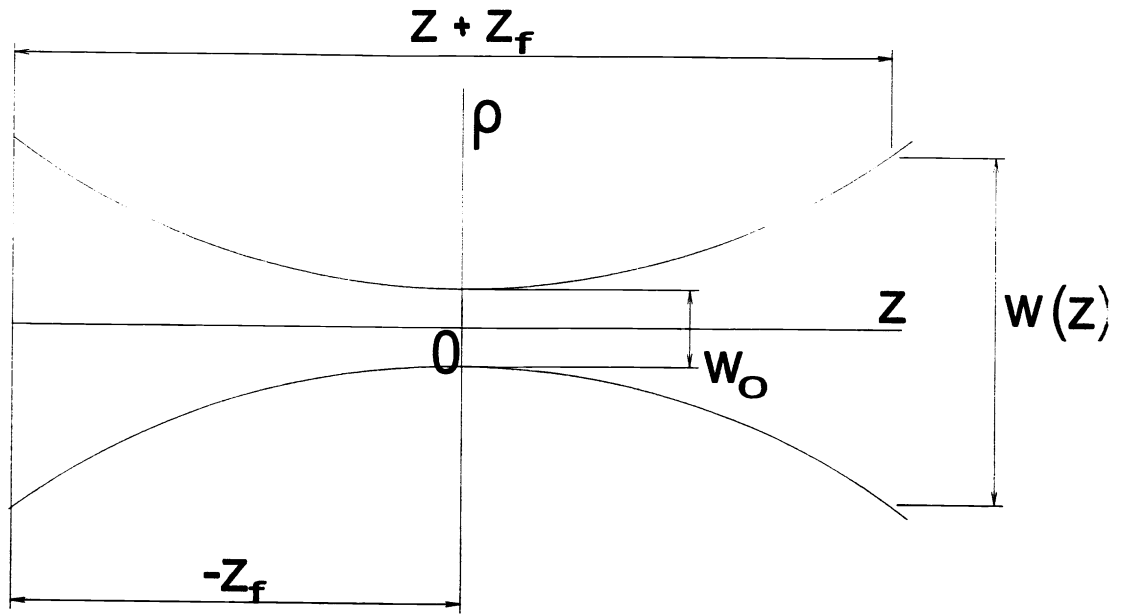
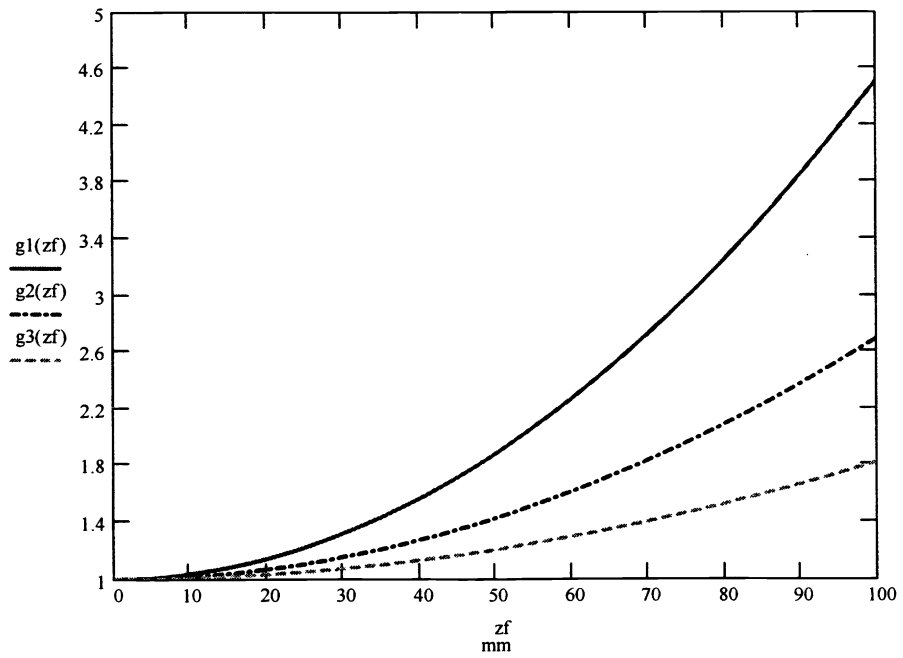


FIG. 3



FLUORESCENT SIGNAL VS. FLUOROPHORE DEPTH

FIG. 4

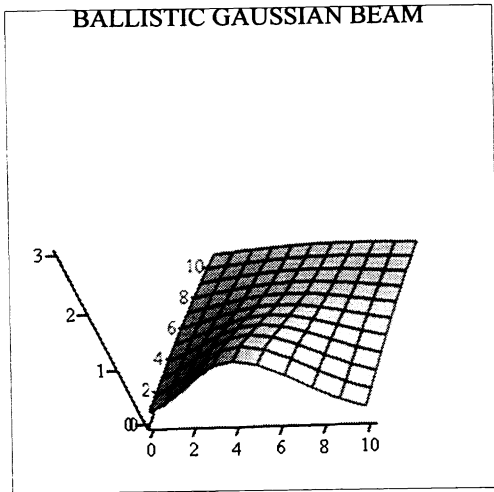


FIG. 5

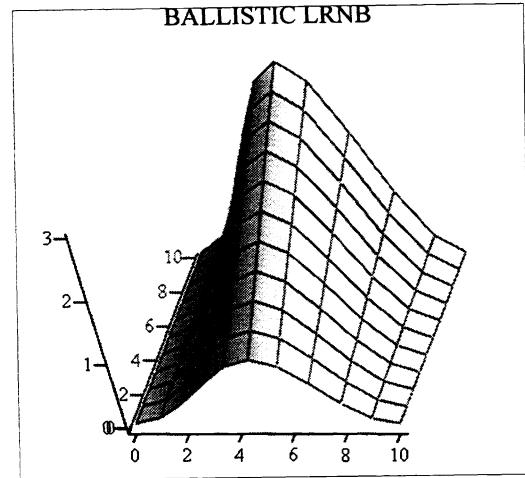
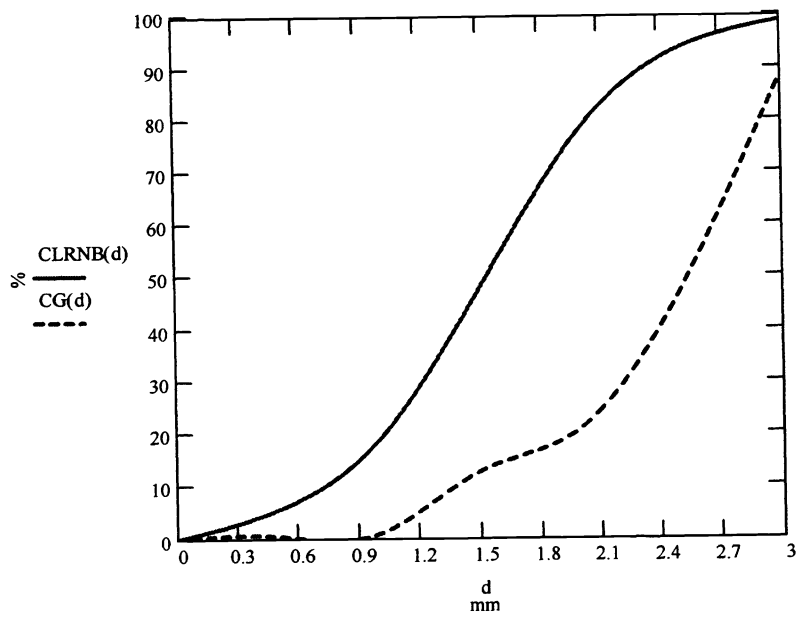


FIG. 6



CONTRAST VS. INHOMOGENEITY SIZE